




Cite this: *Dalton Trans.*, 2025, **54**, 13110

## Self-supporting $\text{Co}_3\text{O}_4/\text{NiFe}_2\text{O}_4$ nanoflowers for efficient oxygen evolution reaction

Ying Wang,<sup>a</sup> Yanghanqi Li,<sup>b</sup> Jun Yu<sup>b</sup> and Yukou Du<sup>✉</sup> 

The construction of high-quality oxygen evolution reaction (OER) catalysts is crucial for the widespread application of hydrogen production technology. Herein, a  $\text{Co}_3\text{O}_4/\text{NiFe}_2\text{O}_4$  nanoflower electrocatalyst with an enhanced metal synergistic effect is reported. The unique nanoflower structure endows the catalyst with fast mass transfer kinetics. The introduction of  $\text{Co}_3\text{O}_4$  not only enhances the multi-metal synergistic effect in  $\text{NiFe}_2\text{O}_4$ , optimizing the adsorption of oxygen-containing intermediates, but also improves the conductivity of the material, facilitating interfacial charge transfer. Accordingly, the  $\text{Co}_3\text{O}_4/\text{NiFe}_2\text{O}_4$  material exhibits extraordinary OER activity ( $\eta_{10} = 236$  mV) and stability. Surprisingly, the  $\text{Co}_3\text{O}_4/\text{NiFe}_2\text{O}_4//\text{Pt/C}$  electrode still demonstrates remarkable performance ( $E_{10} = 1.54$  V) during overall water splitting (OWS) testing. This outstanding electrochemical performance of the  $\text{Co}_3\text{O}_4/\text{NiFe}_2\text{O}_4$  electrocatalyst lays a solid foundation for its potential commercial application.

Received 9th July 2025,  
Accepted 13th August 2025

DOI: 10.1039/d5dt01610j

rsc.li/dalton

## Introduction

The international community has reached a consensus on the urgency of advancing sustainable energy technologies, as global energy scarcity and environmental deterioration continue to escalate.<sup>1–4</sup> The predominant dependence on fossil fuels remains a critical issue, with their combustion releasing massive amounts of greenhouse gases that exacerbate climate change and damage ecosystems.<sup>5,6</sup> Given that fossil fuels formed over geological timescales are being exhausted far faster than natural replenishment rates, transitioning to renewable alternatives is now an imperative strategy for energy security and environmental preservation.<sup>7–9</sup>

Metal-organic frameworks (MOFs), which consist of metal clusters interconnected by organic ligands via coordination bonds, exhibit well-ordered nanostructures with exceptional porosity, extensive surface areas, and remarkable structural integrity.<sup>10–12</sup> Beyond their traditional applications in gas separation, catalytic processes and energy storage systems, MOFs have recently emerged as versatile precursors for oxygen evolution reaction (OER) electrocatalysts. Notable examples include zeolitic imidazolate frameworks (ZIFs),<sup>13,14</sup> Prussian blue analogs (PBAs),<sup>15,16</sup> and carboxylate MOFs.<sup>17,18</sup> Furthermore, MOF-derived composites synthesized through sacrificial template strategies demonstrate superior electrical

conductivity, catalytic performance, and durability compared to pristine MOFs, owing to their tailored multi-metallic compositions.<sup>19–21</sup> As reviewed by Wang *et al.*,<sup>22</sup> the rational design of MOF-based carbonyl materials enables precise control over morphological architectures and pore distributions, while the atomic-level dispersion of metal centers synergizes with coordinating atoms to optimize catalytic efficiency for OER, HER and ORR. Complementary to this, De Villenois *et al.* emphasized that MOF derivatives overcome the inherent limitations of conventional MOFs such as poor electrical transport and thermodynamic instability through innovative synthesis protocols. Furthermore, *in situ* growth on conductive substrates bypasses the requirements of adhesives and significantly improved the interfacial charge transfer kinetics.

Extensive research has established that Ni-Fe bimetallic systems exhibit remarkable catalytic synergy, substantially lowering the overpotential required for OER.<sup>23–25</sup> However, the practical deployment of NiFe-based electrocatalysts is often constrained by their inherently poor charge transport properties. To address this limitation, interfacial engineering of heterostructure materials has proven effective in facilitating electron migration and boosting catalytic kinetics.<sup>26,27</sup> A representative case is Xiao *et al.*'s work, where a NiFe-layered double hydroxide/MOF (NiFe-LDH/MOF) heterojunction was fabricated through sequential synthesis. Advanced characterization techniques identified abundant oxygen vacancies and crystallographic defects in this system, which collectively weakened the binding energy of reaction intermediates (\*OH, \*O). These structural modifications enabled an ultralow overpotential of 275 mV at 100 mA cm<sup>−2</sup>.<sup>28</sup> Similarly, Huang's group designed a hierarchical MoC-Fe@NCNTs heterostructure by pyrolyzing

<sup>a</sup>Department of Pharmacy, Jiangsu Agri-animal Husbandry Vocational College, Taizhou, 225300, P.R. China

<sup>b</sup>College of Chemistry, Chemical Engineering and Materials Science, Soochow University, Industrial Park, Renai Road, Suzhou 215123, P.R. China.

E-mail: duyk@suda.edu.cn

ZIF-8 precursors with iron sources, followed by nitrogen-doped carbon nanotube encapsulation. The strong electronic coupling between metallic Fe and molybdenum carbide at phase boundaries was found to simultaneously enhance OER and hydrogen evolution (HER) activities.<sup>29</sup>

To synergistically combine interface engineering and multi-metal interactions, this work developed a  $\text{Co}_3\text{O}_4/\text{NiFe}_2\text{O}_4$  heterostructure catalyst through hydrothermal calcination treatment of Co-MOF precursors. The three-dimensional (3D) nanoflower structure not only enables thorough exposure of active sites, enhancing the intrinsic activity of the material, but also significantly increases the electrode/electrolyte contact area, thereby accelerating mass transfer kinetics during the electrolysis process. Furthermore, the construction of heterogeneous interfaces induces the redistribution of electrons and accelerates electron transfer across the interfaces, resulting in enhanced catalytic kinetics. Accordingly, the  $\text{Co}_3\text{O}_4/\text{NiFe}_2\text{O}_4$  catalyst demonstrates outstanding OER activity and stability. This material only requires 236 mV to achieve a current density of  $10 \text{ mA cm}^{-2}$  and maintain stable operation for 60 h. More importantly, when it is combined with Pt/C to form a two-electrode system for overall water splitting (OWS), the  $\text{Co}_3\text{O}_4/\text{NiFe}_2\text{O}_4/\text{Pt/C}$  electrode maintains favorable catalytic activity, exhibiting a low potential of merely 1.54 V at  $10 \text{ mA cm}^{-2}$ , along with exceptional stability exceeding 40 h. This study broadens the design ideas for MOFs-derived spinel-type heterojunction electrocatalysts.

## Experimental section

### Synthesis of Co-MOF/NF

$\text{Co}(\text{NO}_3)_2 \cdot 6\text{H}_2\text{O}$  (0.4 mmol) and terephthalic acid (0.5 mmol) were dissolved in 18 mL of DMF with stirring to prepare the precursor solution. To this homogeneous mixture, 1 mL each of absolute ethanol (ET) and ultrapure water (UPW) were introduced dropwise. After 30 min of vigorous stirring, the pre-treated NF substrates were carefully immersed in the solution. The synthesis was carried out in a Teflon-lined autoclave maintained at  $125^\circ\text{C}$  for 12 h under static conditions. The resulting product underwent thorough UPW washing cycles before final drying at  $60^\circ\text{C}$  in an air-circulated oven.

### Synthesis of $\text{Co}_3\text{O}_4/\text{NiFe}_2\text{O}_4$

A homogeneous precursor solution was prepared by ultrasonically dissolving  $\text{Fe}(\text{NO}_3)_3 \cdot 9\text{H}_2\text{O}$  (0.2 mmol),  $\text{Ni}(\text{NO}_3)_2 \cdot 6\text{H}_2\text{O}$  (0.4 mmol),  $\text{NH}_4\text{F}$  (0.7 mmol), and  $\text{CO}(\text{NH}_2)_2$  (1.3 mmol) in 10 mL UPW for 30 min. The pre-synthesized Co-MOF/NF substrate was then immersed in this solution, and hydrothermal growth was performed in a Teflon-lined autoclave at  $120^\circ\text{C}$  for 10 h under static conditions. After cooling naturally, the resulting composite underwent sequential washing cycles with UPW and absolute ethanol before drying at  $60^\circ\text{C}$  overnight. Subsequent thermal treatment involved programmed calcination in static air ( $450^\circ\text{C}$  for 3 h,  $2^\circ\text{C min}^{-1}$ ), yielding the final  $\text{Co}_3\text{O}_4/\text{NiFe}_2\text{O}_4$  heterostructure upon furnace cooling to ambient temperature.

### Synthesis of $\text{Co}_3\text{O}_4/\text{NiO}_x$

The synthesis method was the same as  $\text{Co}_3\text{O}_4/\text{NiFe}_2\text{O}_4$ , except that  $\text{Fe}(\text{NO}_3)_3 \cdot 9\text{H}_2\text{O}$  was not added to the precursor solution.

### Synthesis of $\text{Co}_3\text{O}_4/\text{FeO}_x$

The synthesis method was the same as  $\text{Co}_3\text{O}_4/\text{NiFe}_2\text{O}_4$ , except that  $\text{Ni}(\text{NO}_3)_2 \cdot 6\text{H}_2\text{O}$  was not added to the precursor solution.

### Synthesis of $\text{NiFe}_2\text{O}_4$

$\text{Fe}(\text{NO}_3)_3 \cdot 9\text{H}_2\text{O}$  (0.2 mmol),  $\text{Ni}(\text{NO}_3)_2 \cdot 6\text{H}_2\text{O}$  (0.4 mmol),  $\text{NH}_4\text{F}$  (0.7 mmol), and  $\text{CO}(\text{NH}_2)_2$  (1.3 mmol) were ultrasonically dissolved in 10 mL UPW. The mixture and treated NF were transferred to a Teflon-lined autoclave for hydrothermal treatment at  $120^\circ\text{C}$  for 10 h. After the reaction, the products were washed alternately with UPW and ET and dried for use. Subsequent thermal annealing in ambient atmosphere involved programmed heating to  $450^\circ\text{C}$  ( $2^\circ\text{C min}^{-1}$ ), maintaining this temperature for 3 h before furnace cooling yielded phase-pure  $\text{NiFe}_2\text{O}_4$ .

## Results and discussion

### Physical characterization

The synthesis process of  $\text{Co}_3\text{O}_4/\text{NiFe}_2\text{O}_4$  is shown in Fig. 1. Specifically, in the presence of DMF, the  $-\text{COOH}$  groups in  $\text{H}_2\text{BDC}$  underwent deprotonation at high temperature, generating  $-\text{COO}^-$  anions that coordinated with  $\text{Co}^{2+}$  ions, ultimately leading to the formation of Co-MOF. Subsequently, metal salts of  $\text{Ni}^{2+}$  and  $\text{Fe}^{3+}$  were added, and  $\text{Co}_3\text{O}_4/\text{NiFe}_2\text{O}_4$  was produced through hydrothermal-calcination treatment.

The surface morphology and structure of the materials were analyzed utilizing scanning electron microscopy (SEM) and transmission electron microscopy (TEM). Fig. 2a shows the SEM image of  $\text{NiFe}_2\text{O}_4$ , displaying a three-dimensional nanoflower structure formed by interwoven slender fibers with a rough surface. The SEM images of Co-MOF (Fig. 2b and c) reveal that Co-MOF exhibits dense stacking, which is beneficial for increasing the specific surface area. Meanwhile, the individual sheet-like crystals show orientation characteristics, which is related to the highly polar DMF solvent environment in the reaction system. The introduction of DMF promotes the preferential growth of MOF along specific crystal planes, thereby generating sheet-like or columnar structures. In Fig. 2d, the TEM image of  $\text{Co}_3\text{O}_4/\text{NiFe}_2\text{O}_4$  shows aggregated nanosheet structures with darker central regions, indicating density differences. Meanwhile, Fig. 2e and f demonstrate that  $\text{Co}_3\text{O}_4/\text{NiFe}_2\text{O}_4$  exhibits a three-dimensional nanoflower cluster morphology with relatively regular shapes and nanoscale protrusions on the surface. The dense hierarchical structure optimizes conductivity. In the highly polar DMF solvent environment,  $\text{Co}^{2+}$  and  $\text{H}_2\text{BDC}$  ligands can achieve better dispersion and coordination, and self-assemble into this morphology as the reaction proceeds, which helps enhance the overall activity of the catalyst.<sup>30</sup> As a comparison,  $\text{Co}_3\text{O}_4/\text{FeO}_x$  and  $\text{Co}_3\text{O}_4/\text{NiO}_x$  were also tested by SEM. As illustrated in

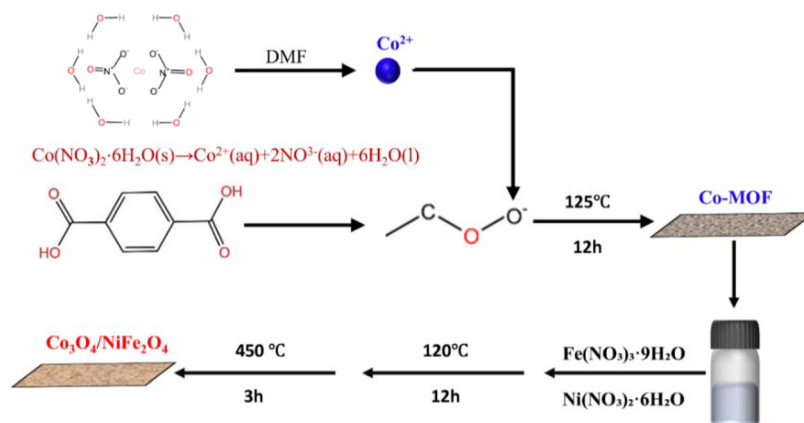


Fig. 1 Schematic of the synthesis of  $\text{Co}_3\text{O}_4/\text{NiFe}_2\text{O}_4$ .

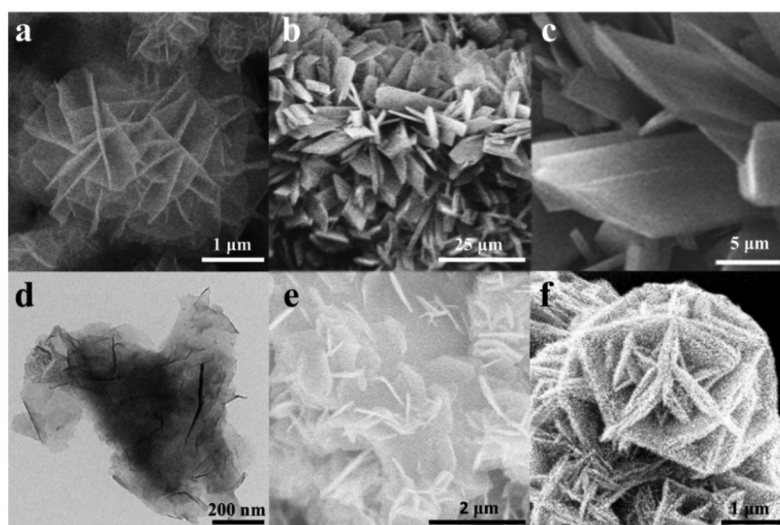


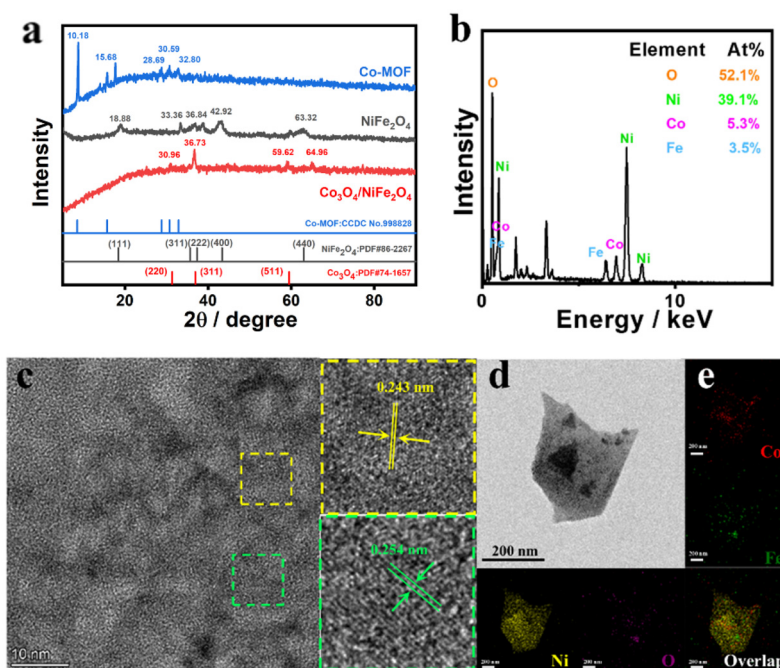
Fig. 2 SEM images of (a)  $\text{NiFe}_2\text{O}_4$ , (b and c)  $\text{Co-MOF}$  and (e and f)  $\text{Co}_3\text{O}_4/\text{NiFe}_2\text{O}_4$ . TEM image of (d)  $\text{Co}_3\text{O}_4/\text{NiFe}_2\text{O}_4$ .

Fig. S1a,  $\text{Co}_3\text{O}_4/\text{FeO}_x$  is mainly composed of numerous thin sheet-like crystals, which are interwoven and stacked to form a loose layered structure with a small number of granular components interspersed, helping to construct porous channels that facilitate electrolyte penetration and ion diffusion during the reaction. In contrast,  $\text{Co}_3\text{O}_4/\text{NiO}_x$  exhibits a more compact and uniform nanostructure, with surfaces composed of fine particles or short rod-like units arranged in a flower-cluster-like pattern (Fig. S1b).

The phase composition and crystal structure of the materials were explored using X-ray diffraction (XRD). For the Co material in Fig. 3a, the diffraction peaks at  $10.18^\circ$ ,  $15.68^\circ$ ,  $28.69^\circ$ ,  $30.59^\circ$  and  $32.80^\circ$  confirm the successful synthesis of the Co-MOF precursor (CCDC no. 998828).<sup>31</sup> Notably, the diffraction peaks at  $64.96^\circ$  in  $\text{Co}_3\text{O}_4/\text{NiFe}_2\text{O}_4$  correspond to  $\text{NiFe}_2\text{O}_4$  (PDF#86-2267), while those at  $30.96^\circ$ ,  $36.73^\circ$  and  $59.62^\circ$  match the characteristic peaks of  $\text{Co}_3\text{O}_4$  (PDF#74-1657).<sup>32,33</sup> These results suggest the successful formation and

coexistence of both phases in the composite. Since the Co-MOF precursor has been completely transformed into  $\text{Co}_3\text{O}_4$ , no diffraction peaks related to the Co-MOF precursor are observed in the XRD pattern of  $\text{Co}_3\text{O}_4/\text{NiFe}_2\text{O}_4$ . Meanwhile, both the energy dispersive X-ray spectroscopy (EDS) pattern and elemental mapping images of  $\text{Co}_3\text{O}_4/\text{NiFe}_2\text{O}_4$  show the presence and uniform distribution of Ni, Co, Fe, and O (Fig. 3b and e), indicating the successful preparation of the  $\text{Co}_3\text{O}_4/\text{NiFe}_2\text{O}_4$  composite. Additionally, the heterogeneous interface of the  $\text{Co}_3\text{O}_4/\text{NiFe}_2\text{O}_4$  material was deeply studied by using high-resolution TEM (HRTEM). In Fig. 3c, there are two distinct lattice fringes, which belong to the (311) plane of  $\text{Co}_3\text{O}_4$  (0.243 nm) and the (311) plane of  $\text{NiFe}_2\text{O}_4$  (0.254 nm) respectively. This result further proves the successful synthesis of the  $\text{Co}_3\text{O}_4/\text{NiFe}_2\text{O}_4$  heterostructure composite.

The composition of the catalyst and its potential advantages in catalytic reactions were further investigated by utilizing X-ray photoelectron spectroscopy (XPS). As shown in



**Fig. 3** (a) XRD patterns of Co-MOF, NiFe<sub>2</sub>O<sub>4</sub> and Co<sub>3</sub>O<sub>4</sub>/NiFe<sub>2</sub>O<sub>4</sub>, (b) EDS spectrum, (c) HRTEM image, (d) HAADF image and (e) elemental mapping images of Co<sub>3</sub>O<sub>4</sub>/NiFe<sub>2</sub>O<sub>4</sub>.

Fig. S3, the survey scan spectrum of Co-MOF evidences the presence of Co and O, with high-resolution Co 2p spectra exhibiting characteristic spin-orbit doublets at 781.2 eV (2p<sub>3/2</sub>) and 797.3 eV (2p<sub>1/2</sub>), accompanied by satellite peaks at 786.5 eV and 803 eV, indicative of predominant Co<sup>2+</sup> oxidation states.<sup>34</sup> Compared with the survey scan spectrum of NiFe<sub>2</sub>O<sub>4</sub>, the survey scan spectrum of Co<sub>3</sub>O<sub>4</sub>/NiFe<sub>2</sub>O<sub>4</sub> shows a distinct Co signal (Fig. 4a and b), indicating the successful introduction of Co<sub>3</sub>O<sub>4</sub>.<sup>35</sup> Detailed analysis of the Co 2p fine structure of Co<sub>3</sub>O<sub>4</sub>/

NiFe<sub>2</sub>O<sub>4</sub> identifies mixed valence states, with binding energies at 780.9 eV (Co<sup>2+</sup> 2p<sub>3/2</sub>) and 797.5 eV (Co<sup>2+</sup> 2p<sub>1/2</sub>) alongside peaks at 779.6 eV (Co<sup>3+</sup> 2p<sub>3/2</sub>) and 794.7 eV (Co<sup>3+</sup> 2p<sub>1/2</sub>) (Fig. 4c). The observed satellite features at 786.4 eV and 803 eV, consistent with XRD and HRTEM results, verified the formation of Co<sub>3</sub>O<sub>4</sub> spinel phase.<sup>36</sup> The Fe 2p spectrum of Co<sub>3</sub>O<sub>4</sub>/NiFe<sub>2</sub>O<sub>4</sub> exhibits characteristic doublets at 710.5 eV (Fe<sup>3+</sup> 2p<sub>3/2</sub>) and 722.5 eV (Fe<sup>3+</sup> 2p<sub>1/2</sub>), showing a 1.7 eV negative shift relative to pure NiFe<sub>2</sub>O<sub>4</sub> (712.2 eV and 724.1 eV), indicating signifi-

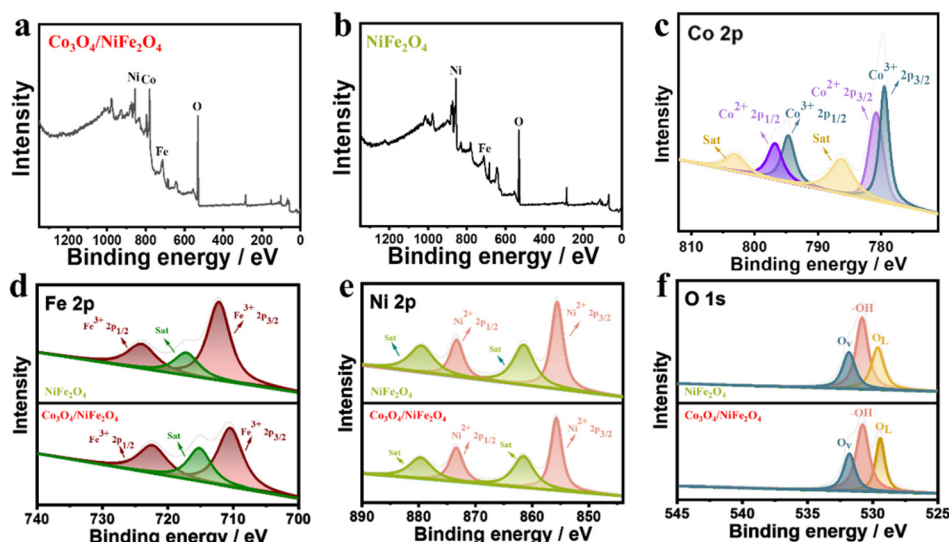


**Fig. 4** XPS spectra of (a and b) survey scan, (d) Fe 2p, (e) Ni 2p and (f) O 1s for Co<sub>3</sub>O<sub>4</sub>/NiFe<sub>2</sub>O<sub>4</sub> and NiFe<sub>2</sub>O<sub>4</sub>; (c) Co 2p for Co<sub>3</sub>O<sub>4</sub>/NiFe<sub>2</sub>O<sub>4</sub>.



cant electronic structure modulation (Fig. 4d). For the Ni 2p region of  $\text{Co}_3\text{O}_4/\text{NiFe}_2\text{O}_4$ , binding energies at 855.6 eV ( $2p_{3/2}$ ) and 873.2 eV ( $2p_{1/2}$ ) confirm  $\text{Ni}^{2+}$  in tetrahedral coordination, with cobalt incorporation preserving the local Ni environment (Fig. 4e).<sup>37</sup> The O 1s spectrum of  $\text{Co}_3\text{O}_4/\text{NiFe}_2\text{O}_4$  shows three major peaks at 529.5, 530.9 and 531.9 eV, attributed to lattice oxygen ( $\text{O}_\text{L}$ ), hydroxyl groups ( $-\text{OH}$ ), and oxygen vacancies ( $\text{O}_\text{v}$ ), respectively (Fig. 4f). Quantitative analysis of the peak area ratios for  $\text{Co}_3\text{O}_4/\text{NiFe}_2\text{O}_4$  reveals increases of 20.7, 26.9 and 18.1% in  $\text{O}_\text{L}$ , M–OH and  $\text{O}_\text{v}$  content, respectively. The enhanced  $\text{O}_\text{L}$  concentration suggests the formation of a more stable spinel structure, improving the overall conductivity. The increased  $-\text{OH}$  groups, rich in hydrophilic moieties, facilitate electrolyte penetration and the formation of intermediates ( $\text{OOH}^*$ ). Meanwhile, the rise in  $\text{O}_\text{v}$  provides additional active sites for catalytic reactions. Collectively, these modifications contribute to enhanced catalytic activity.<sup>38</sup>

The chemical states and surface composition of  $\text{Co}_3\text{O}_4/\text{NiO}_x$  were probed by XPS (Fig. S4), with the survey scan spectrum confirming Co, Ni and O as primary constituents. High-resolution analysis of the Co 2p region reveals characteristic spin-orbit doublets at 779.8 eV ( $\text{Co}^{2+} 2p_{3/2}$ ) and 797.8 eV ( $\text{Co}^{2+} 2p_{1/2}$ ), accompanied by shake-up satellite features,<sup>39</sup> suggesting the coexistence of  $\text{Co}^{2+}/\text{Co}^{3+}$  oxidation states characteristic of the  $\text{Co}_3\text{O}_4$  phase. The Ni 2p spectrum of  $\text{Co}_3\text{O}_4/\text{NiO}_x$  exhibits binding energies at 855.6 eV ( $\text{Ni}^{2+} 2p_{3/2}$ ) and 873.2 eV ( $\text{Ni}^{2+} 2p_{1/2}$ ), indicating Ni maintains its +2-valence state without significant alteration of the spinel coordination environment.<sup>40</sup> The O 1s spectrum (529–533 eV) can be deconvoluted into  $\text{O}_\text{L}$ ,  $-\text{OH}$ , and  $\text{O}_\text{v}$ . The dominant  $\text{O}_\text{L}$  component confirms the stable spinel structure, while the presence of  $\text{O}_\text{v}$  may provide additional active sites for OER. Similarly, XPS analysis of  $\text{Co}_3\text{O}_4/\text{FeO}_x$  displays Co 2p peaks at

781.2 and 798.1 eV, again indicating  $\text{Co}^{2+}$  as the predominant state (Fig. S5b). In Fig. S5c, the Fe 2p spectrum shows characteristic binding energies at 712.8 eV ( $\text{Fe}^{3+} 2p_{3/2}$ ) and 720.1 eV ( $\text{Fe}^{3+} 2p_{1/2}$ ), confirming the presence of  $\text{Fe}^{3+}$ . The O 1s spectrum of  $\text{Co}_3\text{O}_4/\text{FeO}_x$  exhibits similar  $\text{O}_\text{L}$ ,  $-\text{OH}$ , and  $\text{O}_\text{v}$  components as  $\text{Co}_3\text{O}_4/\text{NiO}_x$ , but with higher  $\text{O}_\text{v}$  content, likely resulting from Fe incorporation that promotes oxygen defect formation, thereby enhancing catalytic activity (Fig. S5d).

### Electrocatalytic OER performance

Benefiting from the advantages of the  $\text{Co}_3\text{O}_4/\text{NiFe}_2\text{O}_4$  catalyst in terms of structure and composition, its electrochemical performance in alkaline electrolyte was evaluated using a three-electrode system.<sup>41</sup> As shown in Fig. 5a and b,  $\text{Co}_3\text{O}_4/\text{NiFe}_2\text{O}_4$  exhibits the optimum OER activity ( $\eta_{10} = 236$  mV), significantly outperforming  $\text{Co}_3\text{O}_4/\text{NiO}_x$  ( $\eta_{10} = 260$  mV),  $\text{Co}_3\text{O}_4/\text{FeO}_x$  ( $\eta_{10} = 284$  mV), Co-MOF ( $\eta_{10} = 327$  mV) and  $\text{NiFe}_2\text{O}_4$  ( $\eta_{10} = 344$  mV). This enhanced activity can be attributed to two key factors: 1. The synergistic interaction between Ni and Fe; 2. The optimized electronic structure resulting from  $\text{Co}_3\text{O}_4$  incorporation. Accordingly,  $\text{Co}_3\text{O}_4/\text{NiFe}_2\text{O}_4$  manifests outstanding OER performance compared to most reported catalysts (Fig. 5d and Table S1). The reaction kinetics of the catalysts were further revealed utilizing Tafel slopes (Fig. 5c). Compared with  $\text{Co}_3\text{O}_4/\text{NiO}_x$  (101.71 mV  $\text{dec}^{-1}$ ),  $\text{Co}_3\text{O}_4/\text{FeO}_x$  (108.08 mV  $\text{dec}^{-1}$ ), Co-MOF (115.5 mV  $\text{dec}^{-1}$ ) and  $\text{NiFe}_2\text{O}_4$  (141.76 mV  $\text{dec}^{-1}$ ),  $\text{Co}_3\text{O}_4/\text{NiFe}_2\text{O}_4$  shows the lowest Tafel slope (97.84 mV  $\text{dec}^{-1}$ ), highlighting its excellent catalytic kinetics. The rapid charge transfer reflects exceptional conductivity. The charge transfer resistance of the materials was analyzed by electrochemical impedance spectroscopy (EIS).<sup>42</sup> As shown in Fig. S6, the smallest semicircle radius for  $\text{Co}_3\text{O}_4/\text{NiFe}_2\text{O}_4$  indicates the lowest charge transfer resistance, representing optimal conductivity.

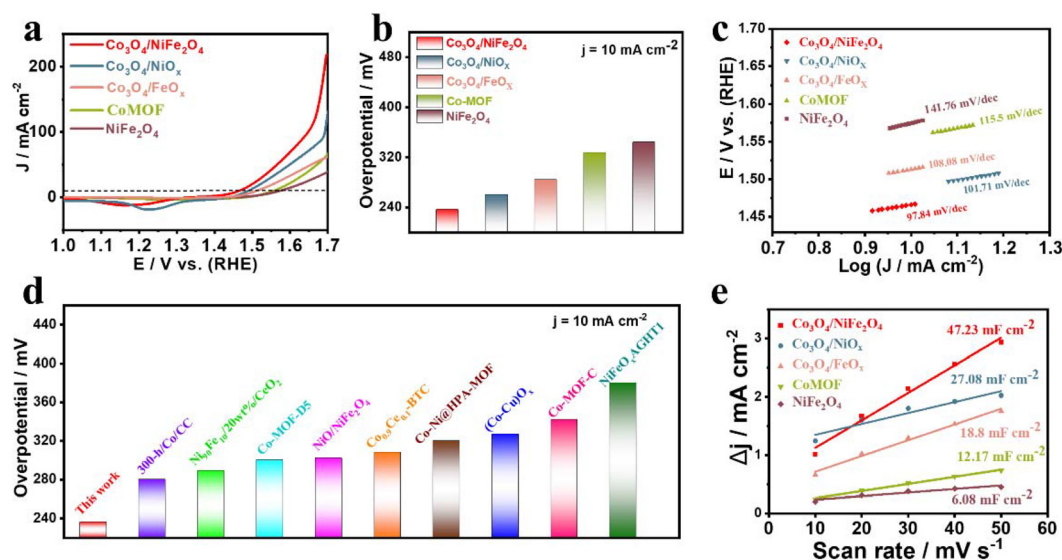


Fig. 5 (a) LSV curves, (b) overpotential comparison at  $10 \text{ mA cm}^{-2}$ , (c) Tafel slope, (d) overpotential comparison with other related catalysts, and (e)  $C_{\text{dl}}$  values of  $\text{Co}_3\text{O}_4/\text{NiFe}_2\text{O}_4$ ,  $\text{Co}_3\text{O}_4/\text{NiO}_x$ ,  $\text{Co}_3\text{O}_4/\text{NiFeO}_x$ , Co-MOF and  $\text{NiFe}_2\text{O}_4$ .

This improvement can be ascribed to the synergistic effect of Ni and Fe surface oxidation states, which effectively reduces interfacial resistance.<sup>43</sup> The electrochemical active surface area (ECSA) represents the effective area of the catalyst participating in the electrolytic reaction, which is proportional to the double-layer capacitance ( $C_{dl}$ ). Therefore, the  $C_{dl}$  value of the material can be calculated to reflect its ECSA. In Fig. 5e,  $\text{Co}_3\text{O}_4/\text{NiFe}_2\text{O}_4$  displays the highest  $C_{dl}$  value ( $47.23 \text{ mF cm}^{-2}$ ), indicating a larger active surface area and greater abundance of catalytic sites.

Furthermore, the operational stability of the catalyst is a critical parameter for evaluating its electrocatalytic performance, as it determines long-term viability. To assess the durability of  $\text{Co}_3\text{O}_4/\text{NiFe}_2\text{O}_4$ , chronoamperometry (CA) and chronopotentiometry (CP) tests were conducted. As illustrated in Fig. 6a, the current density attenuation of the  $\text{Co}_3\text{O}_4/\text{NiFe}_2\text{O}_4$  material is negligible after 20 h of continuous operation, indicating its excellent catalytic stability. Similarly, the CP curve at  $10 \text{ mA cm}^{-2}$  also reveals favorable catalytic stability (Fig. 6b). Furthermore, to explore the possibility of industrial application of the  $\text{Co}_3\text{O}_4/\text{NiFe}_2\text{O}_4$  material, its catalytic stability was tested at  $100 \text{ mA cm}^{-2}$ . As expected, the  $\text{Co}_3\text{O}_4/\text{NiFe}_2\text{O}_4$  electrocatalyst still maintains favorable OER performance under long-term high-current operation, highlighting its extraordinary electrochemical stability (Fig. 6c).

To further confirm the favorable stability of the  $\text{Co}_3\text{O}_4/\text{NiFe}_2\text{O}_4$  material, the changes in surface morphology, phase composition and electronic structure of the  $\text{Co}_3\text{O}_4/\text{NiFe}_2\text{O}_4$  catalyst after the stability test were analyzed utilizing SEM, XRD and XPS. As shown in Fig. S8, the surface morphology of the  $\text{Co}_3\text{O}_4/\text{NiFe}_2\text{O}_4$  material shows no significant change after the stability test, still exhibiting a complete nanoflower structure, highlighting the excellent catalytic stability of this catalyst. Meanwhile, compared with the  $\text{Co}_3\text{O}_4/\text{NiFe}_2\text{O}_4$  material before the stability test, the intensity of the XRD characteristic peaks of this

material only displays a slight weakening even after long-term stability operation (Fig. S9). This phenomenon once again demonstrates the excellent stability of the  $\text{Co}_3\text{O}_4/\text{NiFe}_2\text{O}_4$  catalyst. Furthermore, the long-term stability test causes the Co 2p spectrum in  $\text{Co}_3\text{O}_4/\text{NiFe}_2\text{O}_4$  to shift towards lower binding energy, while the Fe 2p and Ni 2p spectra shift towards higher binding energy, indicating that Co, Fe, and Ni lost electrons, which is consistent with the actual situation (Fig. S10).

The superior catalytic activity and stability of  $\text{Co}_3\text{O}_4/\text{NiFe}_2\text{O}_4$  can be attributed to the following key factors:<sup>44–47</sup>

1. The unique 3D nanoflower structure maximizes the exposure of active sites, enhancing the OER intrinsic activity of the material. Furthermore, this structure also expands the electrode–electrolyte interfacial area, which effectively promotes the entry of reactants and the escape of gases, thereby alleviating localized acidification issues in the electrolyte during prolonged catalytic operation.
2. The construction of heterogeneous interfaces induces the rearrangement of interfacial charges, which significantly accelerates the electron transfer during electrolysis, thus optimizing the reaction kinetics of the material.
3. The enhanced multi-metal synergistic effect effectively modulates the electronic structure of the material and optimizes the adsorption of reaction intermediates, thereby reducing the catalytic reaction energy barrier.
4. The spinel structures of  $\text{Co}_3\text{O}_4$  and  $\text{NiFe}_2\text{O}_4$  effectively inhibit the dissolution of metal cations during the OER process, endowing the  $\text{Co}_3\text{O}_4/\text{NiFe}_2\text{O}_4$  catalyst with exceptional intrinsic catalytic stability.

### Electrocatalytic OWS performance

In view of the outstanding OER performance of the  $\text{Co}_3\text{O}_4/\text{NiFe}_2\text{O}_4$  material, it (anode) and Pt/C (cathode) were assembled into a two-electrode system for overall water splitting (OWS) testing to further evaluate the possibility of its com-

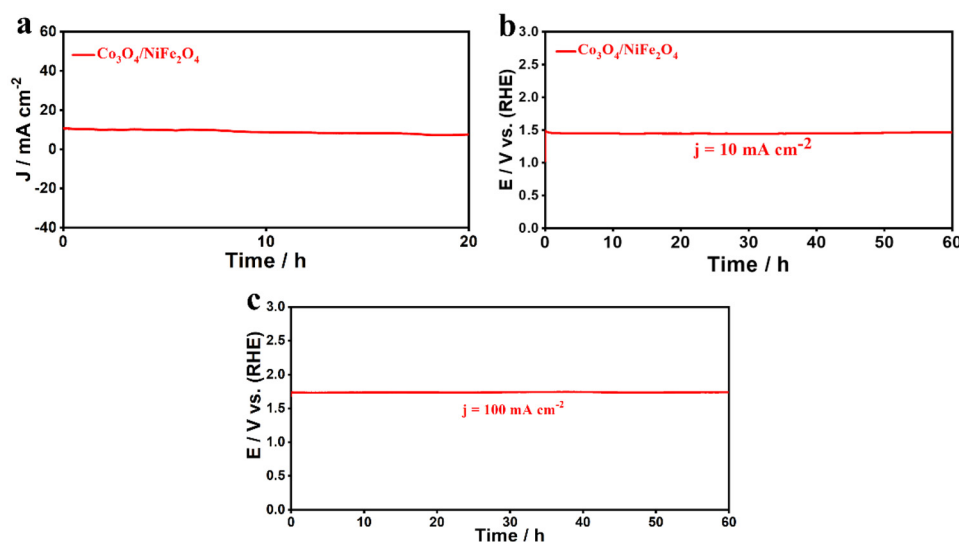


Fig. 6 (a) CA curve at 1.5 V (vs. RHE), (b and c) CP curves of  $\text{Co}_3\text{O}_4/\text{NiFe}_2\text{O}_4$ .

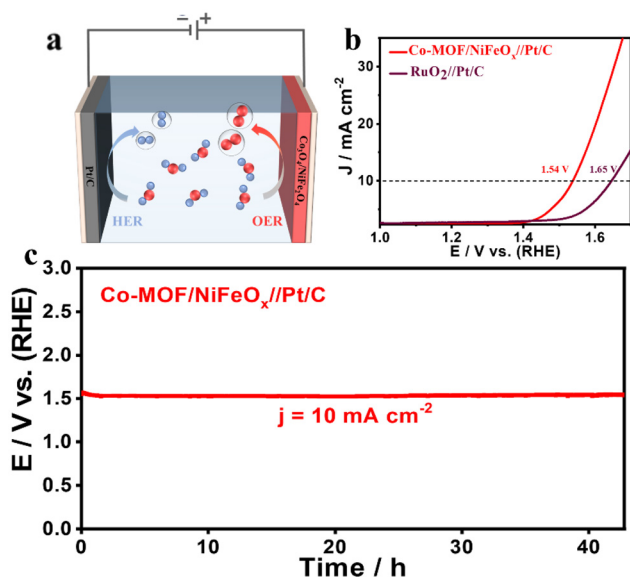


Fig. 7 (a) Schematic diagram of the  $\text{Co}_3\text{O}_4/\text{NiFe}_2\text{O}_4//\text{Pt}/\text{C}$  two-electrode system. (b) LSV curves of  $\text{Co}_3\text{O}_4/\text{NiFe}_2\text{O}_4//\text{Pt}/\text{C}$  and  $\text{RuO}_2//\text{Pt}/\text{C}$ . (c) CP curve of the  $\text{Co}_3\text{O}_4/\text{NiFe}_2\text{O}_4//\text{Pt}/\text{C}$ .

mercial application (Fig. 7a). Fig. 7b shows that the  $\text{Co}_3\text{O}_4/\text{NiFe}_2\text{O}_4//\text{Pt}/\text{C}$  electrode requires only 1.54 V to provide a current density of  $10 \text{ mA cm}^{-2}$ , significantly lower than the commercial  $\text{RuO}_2//\text{Pt}/\text{C}$  (1.65 V), highlighting its brilliant OWS performance. Additionally, the  $\text{Co}_3\text{O}_4/\text{NiFe}_2\text{O}_4//\text{Pt}/\text{C}$  electrode still displays remarkable electrocatalytic performance after 42 h of continuous operation (Fig. 7c). What's more, it still has favorable OWS performance and stability compared to most of the reported catalysts (Table S2). The extraordinary electrochemical activity and stability of the  $\text{Co}_3\text{O}_4/\text{NiFe}_2\text{O}_4$  material endow it with strong potential for industrial applications.

## Conclusions

In summary, the Co-MOF-derived  $\text{Co}_3\text{O}_4/\text{NiFe}_2\text{O}_4$  heterostructure electrocatalyst was successfully constructed via a straightforward hydrothermal-calcination strategy. The XRD pattern and HRTEM image confirm a reasonable coupling of  $\text{Co}_3\text{O}_4$  and  $\text{NiFe}_2\text{O}_4$  at the heterogeneous interface, which effectively facilitates the electron transfer kinetics during electrolysis process. Additionally, the unique nanoflower structure provides abundant active sites for the subsequent catalytic reaction. The synergistic effect between the polymetallic oxides effectively improves the electronic structure of the material and optimizes the adsorption of the reaction intermediates. Benefiting from the above advantages, the  $\text{Co}_3\text{O}_4/\text{NiFe}_2\text{O}_4$  material exhibits outstanding OER activity ( $\eta_{10} = 236 \text{ mV}$ ) and stability. What's more, when  $\text{Co}_3\text{O}_4/\text{NiFe}_2\text{O}_4$  is assembled with Pt/C into a two-electrode system for OWS testing, it still displays impressive catalytic performance ( $E_{10} = 1.54 \text{ V}$ ). This work provides a practical and feasible approach for the preparation of non-precious metal catalysts derived from MOFs.

## Author contributions

Ying Wang: writing – original draft, methodology, software. Yanghanqi Li: validation, investigation. Jun Yu: formal analysis. Yukou Du: supervision, writing – review & editing.

## Conflicts of interest

The authors declare that they have no known competing financial interests or personal relationships that could have appeared to influence the work reported in this paper.

## Data availability

The data that support the findings of this study are available from the corresponding author, upon reasonable request.

Some of the data supporting the findings of this article have been included as part of the SI. See DOI: <https://doi.org/10.1039/d5dt01610j>.

## Acknowledgements

This study was funded by Jiangsu Agri-Animal Husbandry Vocational College Scientific Research Project (NSF2025ZR07); Major Basic Research Project of the Natural Science Foundation of the Jiangsu Higher Education Institutions (24KJA230001); 333 High-Level Talent Training Project of Jiangsu Province.

## References

- I. Gul, M. Sayed, T. Saeed, F. Rehman, A. Naeem, S. Gul, Q. Khan, K. Naz and M. U. Rehman, *Coord. Chem. Rev.*, 2024, **511**, 215870.
- H. J. Huang, M. M. Yan, C. Z. Yang, H. Y. He, Q. G. Jiang, L. Yang, Z. Y. Lu, Z. Q. Sun, X. T. Xu, Y. Bando and Y. Yamauchi, *Adv. Mater.*, 2019, **31**, 1903415.
- Y. Zhang, Y. Y. Zhou, D. L. Sun, Y. X. Nie, D. Y. Wu, L. Ban, B. Tang, S. Yang, H. Li, T. Y. Ma and H. Zhang, *Coord. Chem. Rev.*, 2025, **527**, 216395.
- J. L. Du, D. L. Xiang, K. X. Zhou, L. C. Wang, J. Y. Yu, H. H. Xia, L. L. Zhao, H. Liu and W. J. Zhou, *Nano Energy*, 2022, **104**, 107875.
- A. Ray, S. Sultana, L. Paramanik and K. M. Parida, *J. Mater. Chem. A*, 2020, **8**, 19196–19245.
- N. Han, P. Y. Liu, J. Jiang, L. H. Ai, Z. P. Shao and S. M. Liu, *J. Mater. Chem. A*, 2018, **6**, 19912–19933.
- H. H. Zhang, Y. Fu, H. T. Nguyen, B. Fox, J. H. Lee, A. K. T. Lau, H. Zheng, H. Lin, T. Y. Ma and B. H. Jia, *Coord. Chem. Rev.*, 2023, **494**, 215272.
- N. Zaman, N. Iqbal and T. Noor, *Arabian J. Chem.*, 2022, **15**, 103906.
- K. Zahra, T. Noor, N. Iqbal and N. S. Akbar, *J. Energy Storage*, 2024, **88**, 111565.

- 10 T. Z. Wang, X. J. Cao and L. F. Jiao, *Small*, 2021, **17**, 202004398.
- 11 W. Liang, Y. Li, N. Zhang, J. Li, S. Li, Z. Wu and Y. Du, *Inorg. Chem.*, 2024, **63**, 14691–14698.
- 12 X. R. Tang, N. Li and H. Pang, *Green Energy Environ.*, 2022, **7**, 636–661.
- 13 M. A. Mohamud and A. B. Yurtcan, *Int. J. Hydrogen Energy*, 2021, **46**, 33782–33800.
- 14 L. L. Yin, X. Du, C. Z. Di, M. W. Wang, K. M. Su and Z. H. Li, *Chem. Eng. J.*, 2021, **414**, 128809.
- 15 Y. R. Ji, Y. F. Guo, X. Liu, P. F. Wang and T. F. Yi, *Chem. Eng. J.*, 2023, **471**, 144743.
- 16 H. Sun, S. Yu, X. Gu, J. Yu, J. Li, W. Liang, Z. Wu, T. Liu and Y. Du, *J. Colloid Interface Sci.*, 2025, **691**, 137356.
- 17 F. Z. Sun, H. Xu, W. Zhu, C. Lu, L. Ren, L. A. Chong and J. X. Zou, *Int. J. Hydrogen Energy*, 2023, **48**, 3942–3951.
- 18 Y. W. Liu, L. R. Wang, C. C. Liu, J. Kresse, M. Deconinck, R. Hübner, D. Mikhailova, Y. Vaynzof, X. M. Zhang and A. Eychemüller, *ACS Catal.*, 2025, **15**, 9353–9363.
- 19 X. L. Wang, H. Xiao, A. Li, Z. Li, S. J. Liu, Q. H. Zhang, Y. Gong, L. R. Zheng, Y. Q. Zhu, C. Chen, D. S. Wang, Q. Peng, L. Gu, X. D. Han, J. Li and Y. D. Li, *J. Am. Chem. Soc.*, 2018, **140**, 15336–15341.
- 20 M. Liu, L. Z. Qiao, B. B. Dong, S. Guo, S. Yao, C. Li, Z. M. Zhang and T. B. Lu, *Appl. Catal., B*, 2020, **273**, 119066.
- 21 Y. H. Qian, I. A. Khan and D. Zhao, *Small*, 2017, **13**, 1701143.
- 22 H. F. Wang, L. Y. Chen, H. Pang, S. Kaskel and Q. Xu, *Chem. Soc. Rev.*, 2020, **49**, 1414–1448.
- 23 Y. Yang, Y. C. Xie, Z. H. Yu, S. S. Guo, M. W. Yuan, H. Q. Yao, Z. P. Liang, Y. R. Lu, T. S. Chan, C. Li, H. L. Dong and S. L. Ma, *Chem. Eng. J.*, 2021, **419**, 129512.
- 24 H. Z. Ren, H. Liu, R. T. Qin, H. C. Fu, W. X. Xu, R. Jia, J. Jiang, Y. Z. Yang, Y. T. Xu, B. R. Zeng, C. H. Yuan and L. Z. Dai, *J. Colloid Interface Sci.*, 2025, **680**, 976–986.
- 25 G. S. Liu, F. Xie, X. Cai and J. Y. Ye, *ACS Catal.*, 2024, **14**, 8652–8665.
- 26 H. W. Zhao, J. C. Liang and Y. Zhao, *J. Alloys Compd.*, 2022, **907**, 164479.
- 27 J. Yu, X. Gu, H. Sun, N. Zhang, S. Hata, T. Liu, Z. Wu, Y. Shiraishi and Y. Du, *J. Colloid Interface Sci.*, 2025, **700**, 138429.
- 28 M. J. Xiao, C. Wu, J. W. Zhu, C. T. Zhang, Y. Li, J. Lyu, W. H. Zeng, H. W. Li, L. Chen and S. C. Mu, *Nano Res.*, 2023, **16**, 8945–8952.
- 29 M. H. Huang, S. H. Zhou, D. D. Ma, W. B. Wei, Q. L. Zhu and Z. G. Huang, *Chem. Eng. J.*, 2023, **473**, 145170.
- 30 L. T. Zhao, C. H. Fu, L. X. Luo, J. B. You, L. An, X. H. Yan, S. Y. Shen and J. L. Zhang, *Appl. Catal., B*, 2022, **318**, 121831.
- 31 Z. Zou, T. Wang, X. Zhao, W.-J. Jiang, H. Pan, D. Gao and C. Xu, *ACS Catal.*, 2019, **9**, 7356–7364.
- 32 A. X. Shan, X. Wu, J. Lu, C. P. Chen and R. M. Wang, *CrystEngComm*, 2015, **17**, 1603–1608.
- 33 I. Ahmed, S. G. Dastider, R. Biswas, A. Roy, K. Mondal and K. K. Haldar, *ACS Appl. Nano Mater.*, 2024, **7**, 4035–4050.
- 34 X. S. Hu, H. P. Hu, C. Li, T. Li, X. B. Lou, Q. Chen and B. W. Hu, *J. Solid State Chem.*, 2016, **242**, 71–76.
- 35 Y. H. Q. Li, W. Y. Liang, N. N. Zhang, J. Li, Z. Y. Wu, C. Q. Wang and Y. K. Du, *Int. J. Hydrogen Energy*, 2024, **95**, 832–839.
- 36 D. He, X. Y. Song, W. Q. Li, C. Y. Tang, J. C. Liu, Z. J. Ke, C. Z. Jiang and X. H. Xiao, *Angew. Chem., Int. Ed.*, 2020, **59**, 6929–6935.
- 37 C. Mahala, M. D. Sharma and M. Basu, *Electrochim. Acta*, 2018, **273**, 462–473.
- 38 G. Liu, K. F. Wang, X. S. Gao, D. Y. He and J. P. Li, *Electrochim. Acta*, 2016, **211**, 871–878.
- 39 J.-C. Gan, L. Zhang, J.-J. Feng, Y.-C. Shi, X.-S. Li and A.-J. Wang, *J. Colloid Interface Sci.*, 2025, **687**, 24–35.
- 40 J.-C. Gan, Z.-F. Jiang, K.-M. Fang, X.-S. Li, L. Zhang, J.-J. Feng and A.-J. Wang, *J. Colloid Interface Sci.*, 2025, **677**, 221–231.
- 41 B. Dong, M. X. Li, X. Shang, Y. N. Zhou, W. H. Hu and Y. M. Chai, *J. Mater. Chem. A*, 2022, **10**, 17477–17487.
- 42 L. Liu, Y. Q. Ou and D. Sun, *Chem. Eng. J.*, 2021, **426**, 130063.
- 43 T. N. Luong, T. L. L. Doan, P. M. Bacirhonde and C. H. Park, *Int. J. Hydrogen Energy*, 2025, **99**, 1108–1118.
- 44 N. Chen, S. Che, H. Liu, G. Li, N. Ta, F. Jiang Chen, B. Jiang, N. Wu, Z. Li, W. Yu, F. Yang and Y. Li, *J. Colloid Interface Sci.*, 2023, **638**, 582–594.
- 45 X. Wang, L. Sun, L. Yang, J. Zhao and Q. Xu, *Adv. Funct. Mater.*, 2024, **34**, 2314247.
- 46 M. Qi, H. Tong, G. Li, X. Zheng, Y. Liu, C. Ye, Z. Yan and D. Jiang, *J. Colloid Interface Sci.*, 2025, **684**, 181–188.
- 47 K. Huang, J. Xia, Y. Lu, B. Zhang, W. Shi, X. Cao, X. Zhang, L. M. Woods, C. Han, C. Chen, T. Wang, J. Wu and Y. Huang, *Adv. Sci.*, 2023, **10**, 2300094.